Vacuum 226 (2024) 113284

Contents lists available at ScienceDirect

Vacuum

journal homepage: www.elsevier.com/locate/vacuum

Enhanced wettability of gallium-based liquid metal alloys on copper films by promoting intermetallic reactions

Jianxiao Shen [a,b], Peng Guo [b,**], Shiying Li [c], Wei Yang [b], Cheng Zhang [a], Aiying Wang [b,*]

[a] International Sci. & Tech. Cooperation Base of Energy Materials and Application, College of Chemical Engineering, Zhejiang University of Technology, Hangzhou, 310014, China
[b] Key Laboratory of Advanced Marine Materials, Ningbo Institute of Materials Technology and Engineering, Chinese Academy of Sciences, Ningbo, 315201, China
[c] Key Laboratory of Magnetic Materials and Devices, Ningbo Institute of Materials Technology and Engineering, Chinese Academy of Sciences, Ningbo, 315201, China

ARTICLE INFO

Handling Editor: Prof. L.G. Hultman

Keywords:
Gallium-based liquid metals
PDMS
Cu film
Microtructure
Intermetallic reactions

ABSTRACT

Gallium-based liquid metal alloys (LMs) have promising prospects as circuit components for flexible electronics, while, their high surface tension is now challenging for wetting of LMs on polymer surfaces and further patterning. In this study, we prepared functional Cu thin films on PDMS to enhance wettability of EGaIn liquid metal, using metal reaction-enhanced wetting. By adjusting the deposition pressure for Cu film deposition and introducing silicon-bound PDMS, both surface characteristics and microstructures of the Cu films change greatly. The corresponding contact angle of EGaIn can be tuned from 19° to 79.5°. The folded texture of the Cu film surface reduces the actual contact area, leading to an increase in the contact angle. The higher $I_{(111)}/I_{(200)}$ ratio in the Cu films improves the surface wettability, probably due to the fact that the (111)-phase orientation promotes the formation of $CuGa_2$ reaction products. This tunable wettability of LMs is expected to improve the performance of flexible electronic devices.

1. Introduction

Flexible circuit conductors and electrodes play a crucial role in the functionality of wearable electronics and devices [1–5] as they enable signal transmission even during bending and deformation. Currently, there are two primary techniques employed for fabricating this flexible circuit components. One approach involves the integration of non-stretchable active materials, such as carbon nanotubes, graphene, and metal nanowires, with flexible polymers to fabricate stretchable composite electrodes. For instance, carbon-based stretchable composite electrodes can achieve a remarkable maximum stretchability exceeding 100 %, albeit their electrical conductivity typically remains below 80 S/m [5–7]. Contrast, incorporating various structural patterns such as corrugated, island-bridge, and lattice structures in inorganic semiconductors and metal thin-film materials enables the creation of high-conductivity flexible electrodes. However, these fabricated electrodes encounter the practical bottleneck instability of electrical properties under significant deformation, typically up to a maximum of 20–30 % [4,8,9]. Therefore, it is still an opening challenge to develop stretchable and flexible conductors that for superior strain recovery capabilities, high stability, and conductivity under substantial deformation in wide applications [10–12].

Liquid metals (LMs) refer to liquid alloys and elemental metals that remain in a liquid state at room temperature or slightly elevated temperatures, possessing advantages such as fluid deformability and significant conductivity [13–17]. Among various LMs, gallium-based liquid metals attract much interest due to their good biocompatibility. Therefore, researchers consider the combination of gallium-based liquid metal and polymers a highly promising solution for developing high-performance stretchable conductors. However, the surface tension of LMs is significantly higher(approximately 720 mN/m [18–20]) compared to most polymers with a surface tension below 50 mN/m [21–25], posing a major challenge in wetting LMs onto polymers.

Therefore, the wetting of LMs on polymer surfaces and further patterning remains an unresolved issue in this field. Currently, four methods are being investigated to address this issue: direct writing [26,27], stencil printing [28–30], molding/microfluidic injection [31–33], and selective wetting technology (SWT) [34–39]. Among these techniques, SWT refers to a method of forming patterns by selectively wetting substrates with liquid metals of different wetting properties,

* Corresponding author.
** Corresponding author.
E-mail addresses: guopeng@nimte.ac.cn (P. Guo), aywang@nimte.ac.cn (A. Wang).

https://doi.org/10.1016/j.vacuum.2024.113284
Received 16 February 2024; Received in revised form 29 March 2024; Accepted 9 May 2024
Available online 10 May 2024

resulting in hydrophilic regions and hydrophobic regions. Typically, a high surface energy metal film is deposited on the polymer surface, and the desired pattern structure is prepared using existing metal film patterning methods, such as photolithography and femtosecond laser. The liquid metal is then selectively wetted on the metal pattern structure, while not wetting the polymer. This method is expected to surpass the resolution limit of liquid metal patterning while remaining compatible with large-scale industrial production. Therefore, SWT has recently garnered considerable attention.

For example, Yu Ra Jeong et al. [37] employed magnetron sputtering to deposit an Au film on PDMS, resulting in a significant reduction of the GaInSn contact angle from 130° to 27°. Li et al. [40] introduced a selective liquid metal plating method by electroplating Cu onto PDMS, enabling the fabrication of circuit patterns with a minimum width of approximately 2 μm. Kim et al. [41] investigated the enhanced wetting characteristics of textured metal surfaces using gallium-based liquid metal alloys. They found that EGaIn, an eutectic mixture of indium and gallium, exhibited complete and spontaneous wetting behavior on post-shaped and pyramidal metal surfaces. The wetting properties of liquid metals are typically influenced by their composition and morphology. However, due to limited research on reactive wetting and interfacial structure, the underlying mechanism governing wetting phenomena remains unresolved and poses challenges.

In this study, we prepared a series of Cu films on PDMS by employing PVD magnetron sputtering to enhance the wettability of EGaIn. Compared with other surface techniques, the PVD magnetron sputtering technique has the advantages of low deposition temperature, fast deposition rate, and the ability to achieve uniform and dense film deposition over large areas. Especially, by precisely adjusting deposition parameters during PVD magnetron sputtering, the morphology and microstructure of the film can be effectively tailored [42,43], and its low-temperature characteristic allow the use of organic flexible substrates to maximize their flexibility [44,45]. This is important for the deposition of Cu films on flexible polymer surfaces. By adjusting the deposition pressure for Cu film deposition and introducing silicon substrate to constraint the deformation of PDMS, the surface morphologies and microstructures of the Cu films changed, their roles on the wetting behavior of LMs were investigated, the intermetallic reactions between the Cu film and LMs, and related wetting mechanism were also discussed.

2. Experimental

2.1. Preparation of Cu films

The PDMS (KRN series, Hangzhou Guijin New Material Technology Co.) with a thickness of 200 μm was used as the substrate. To investigate the effect of PDMS deformation during film deposition on the morphology and microstructure of Cu films, PDMS-attached Si wafers were also used as the substrate [46], referred to as PDMS/Si. A multi-target DC magnetron sputtering system was used to deposit the Ti transition layer and Cu layer on both PDMS and PDMS/Si substrates orderly, with a circular target (diameter of 50.8 mm, thickness of 5 mm, purity of 99.99 %). Here, the Ti layer was used to improve the adhesion strength between the Cu layer and the PDMS substrate. The Cu target was connected to a high-power pulsed magnetron sputtering (HiPIMS) power supply, and the Ti target was connected to a direct current magnetron sputtering (DCMS) power supply. The target-to-substrate distance was kept at 7 cm, and the base pressure of the vacuum chamber was less than 1×10^{-3} Pa.

Before deposition, to remove surface contaminants, all substrates were etched by oxygen plasma for 90 s, with an operating power of 60 W and a pressure of 2.7 Pa. Then, under a 100 W DCMS power supply and a 0.5 Pa pressure, the Ar precursor was introduced into the chamber, and the Ti target was ignited. The deposition time for the Ti transition layer was 36 s, with a thickness of 10 ± 2 nm. Then, the Cu layer was deposited, with HiPIMS process parameters of 100 W, 400 Hz, 100 μs pulse width, and 4 % duty cycle. During the Cu layer deposition, the operating Ar gas pressure was set as 0.5 Pa, 1.0 Pa, 1.5 Pa, 2.0 Pa, and 2.5 Pa, while the corresponding sputtering time was also adjusted to ensure the identical thickness of 100 ± 10 nm. The schematic diagram of the multi-target magnetron sputtering setup used to deposit Ti and Cu films is shown in Fig. 1(a), and the schematic structure of the PDMS sample and the PDMS/Si sample are shown in Fig. 1 (b) and (c).

2.2. Characterization methods

A Quanta 250 FEG scanning electron microscope (SEM) equipped with energy dispersive spectroscopy (EDS) was used to investigate the surface morphology and composition of the sample, with a voltage of 2 kV and a current of 0.25 pA.

The wrinkling and folding patterns and surface roughness of the test samples were studied using a scanning probe microscope (Dimension ICON, Bruker, USA) instrument. The scanning range was 50 × 50 μm.

The phase composition of the samples was determined by a Brucker D8-Advance X-ray diffractometer (XRD) at Cu Kα radiation (wavelength λ = 0.15406 nm). The instrument had a tube voltage and current of 40 kV and 40 mA, respectively, with a scan step of 0.02° and an acquisition time of 0.3 s per step.

Talos F200x transmission electron microscope (TEM) was used to analyze the cross-section morphology and microstructure of the test samples before and after wetting.

The liquid metal consists of a mixed gallium and indium, with a mass ratio of 75:25 (purity 99.99 %, Beijing Founde Star Sci. & Technol. Co., Ltd.). Under the protection of nitrogen at 60 °C, the mixture was heated and stirred for 30 min to obtain liquid metal EGaIn.

A Dataphyscis DCAT21 contact angle meter was used to measure the contact angles of LMs on the test samples. The test sample and the cover glass are placed in a glass chamber with dimensions of 10 cm × 10 cm × 10 cm. A 3–5 μL EGaIn droplet is dropped on the substrate through a 0.5 mm diameter syringe. At the same time, HCl solution is dropped on the cover glass at the edge, and the HCl vapor evaporates within 10 s, filling the chamber to eliminate the oxide layer on the surface of the EGaIn and Cu film. To reduce experimental errors, at least three points are taken for repeated testing of each sample, and the average value is calculated.

3. Results and discussion

3.1. Surface morphology of metal films

The surface morphology of the Cu film is shown in Fig. 2. Fig. 2(a) and (c) are nano-scale scanning electron microscope (SEM) images, and Fig. 2(b) and (d) are micron scale Atomic force microscope (AFM) images. Fig. 2(a) presents a SEM image of the Cu film on PDMS, wherein Figs. 2(a-1) illustrates that the Cu film deposited on the PDMS substrate at a pressure of 0.5 Pa exhibits a uniform and fine grain structure. As the deposition pressure increases to 1.0 Pa (Fig. 2(a-2)), the surface becomes smooth. At 1.5 Pa (Figs. 2(a-3)), some cavities and cracks start to emerge on the surface, while at pressures of 2.0 Pa and 2.5 Pa (Figs. 2(a-4) and Fig. (a-5)), cauliflower-shaped structures along with increasing cracks can be observed on the surface. Fig. 2(c), demonstrates the surface morphology of the Cu film on PDMS/Si, where a similar trend is observed as that of the PDMS substrate when subjected to increasing deposition pressure conditions. Due to constraints imposed by the underlying wafer [46], cracking occurs earlier at a deposition pressure of 1.5Pa(Figs. 2(c-3)), and higher density is achieved under certain deposition pressure(Figs. 2(c-4) and Fig. 2(c-5)). The results show that both the substrate and the deposition conditions of metallic films can have a significant impact on their mechanical properties; therefore, designers should consider these factors when utilizing such films in flexible electronic devices.

The wrinkling and folding patterns play a crucial role in determining

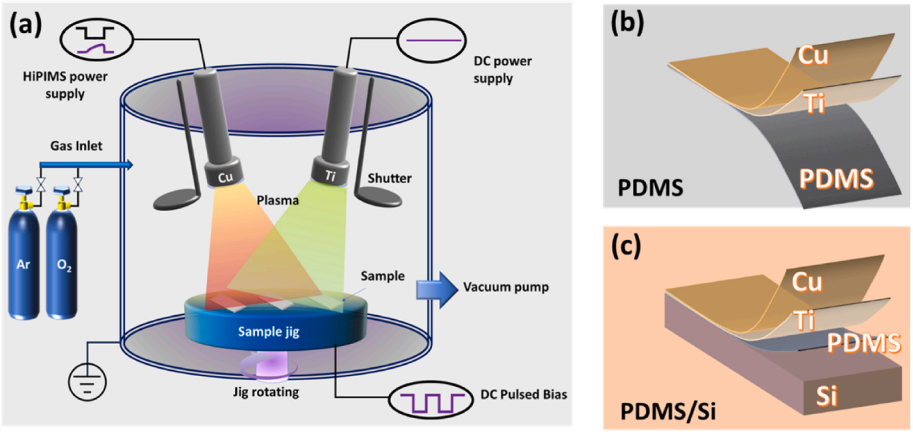

Fig. 1. (a)Schematic diagram of the deposition system for film, (b) Schematic of PDMS sample structure, (c) Schematic of PDMS/Si sample structure.

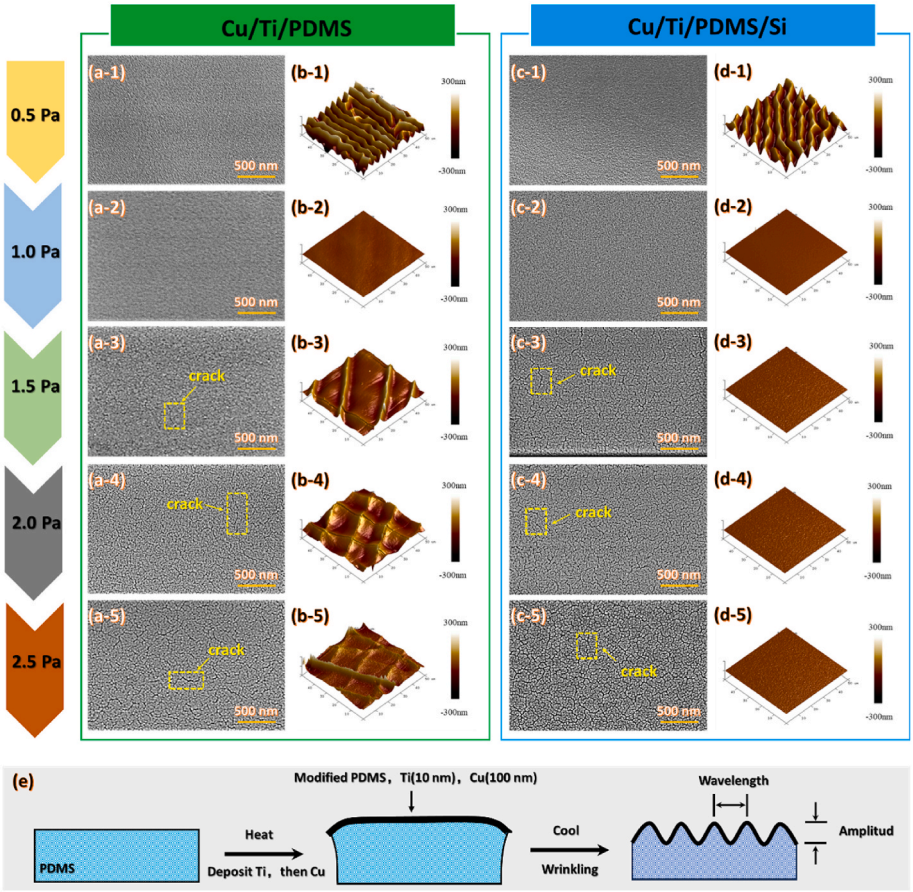

Fig. 2. SEM and AFM images of the samples on (a), (b) PDMS and (c), (d) PDMS/Si substrate at 0.5 Pã2.5 Pa deposition pressure and (e) schematic diagrams of the formation of pleated and folded structures [47].

the wetting behavior [48,49]. These patterns primarily result from residual stress in the films and variations in mechanical properties between metal films and the underlying PDMS [47,50,51]. As depicted in Fig. 2(e), due to the thermal radiation and particle bombardment during film deposition, the temperature of PDMS substrate will increase significantly, resulting in its thermal expansion and the tensile stress in the metal film. After deposition, under the ambient temperature, the PDMS substrate is thermally contracted and the metal film exhibits compressive stress. Under various deposition process, the metal film can have different stress state. With appropriate pressure, the metal film could have a low stress and show smooth surface, once the total stress exceeds a certain critical value, wrinkle or crack can appear to release stress in the films, resulting in crumbling of the film. The fold wavelength represents the distance between two adjacent folding peaks, whereas amplitude refers to the distance between peaks and valleys.

The AFM images presented in Fig. 2 provide an insight into the characteristics of the test samples. At a pressure of 0.5 Pa (Figs. 2(b-1)), distinct folded structures with a wavelength of approximately 4.89 μm and an amplitude of 302.61 nm can be observed on the surface of PDMS samples. Further details are provided in Table 1. In contrast, at a pressure of 1.0 Pa, no folding or wrinkling patterns are visible (Fig. 2(b-2)). The surface appears smooth without any noticeable features. However,

Table 1
Roughness, wavelength, and amplitude of Cu films.

Pressure Substrate		0.5Pa	1.0Pa	1.5Pa	2.0Pa	2.5Pa
PDMS	Ra (nm)	87.53 ± 2.41	6.24 ± 0.41	36.90 ± 1.80	35.37 ± 2.00	29.33 ± 1.40
	Wavelength (μm)	4.89 ± 0.08	18.96 ± 1.25	24.51 ± 0.18	18.07 ± 0.09	14.94 ± 0.18
	Amplitude (nm)	302.61 ± 7.84	14.71 ± 3.11	138.4 ± 5.25	99.59 ± 2.02	87.75 ± 6.03
PDMS/ Si	Ra (nm)	75.43 ± 9.01	1.30 ± 0.48	2.08 ± 0.46	1.56 ± 0.33	1.90 ± 0.43
	Wavelength (μm)	4.28 ± 0.11	> 50			
	Amplitude (nm)	300.14 ± 8.37	5.76 ± 1.53	/		

within the pressure range of 1.5–2.5 Pa, a ridge or quadrilateral feature reemerges on the surface. Table 1 includes corresponding average roughness (Ra) values that demonstrate a decrease from the maximum value of 87.53 nm at a pressure of 0.5 Pa to the minimum value of 6.24 nm at a pressure of 1 Pa. Within the pressure range of 1.5–2.5 Pa, the roughness stabilizes within an average range between 30 and 40 nm.

The AFM images in Figs. 2(d-1) depict metal films on PDMS/Si. At a pressure of 0.5 Pa, the surface exhibits conventional wrinkles with a wavelength of approximately 6.37 μm and an amplitude of around 300.14 nm. As the pressure increases beyond 1.0 Pa, the surface becomes significantly smoother, as shown in Fig. 2(d-2) to (d-5). The corresponding roughness average (Ra) values presented in Table 1 indicate that at 0.5 Pa, a maximum value of 75.43 nm is achieved, followed by a rapid decrease and stabilization at approximately 2 nm for deposition pressure ranging from 1.0 Pa to 2.5 Pa.

According to the SEM and AFM results described above, the Cu films on both substrates exhibit similar morphological characteristics with increasing deposition pressure. As the deposition pressure increases, there is a higher frequency of collisions between deposited atoms, leading to a decrease in deposition energy and nucleation location. Consequently, larger particles form on the substrate surface [52,53]. Moreover, the reduced influx of adsorbed atoms facilitates their surface diffusion, resulting in larger particles. When deposited under identical pressures, the metal film formed on PDMS demonstrates coarser properties compared to that formed on PDMS/Si. This disparity arises from the lesser deformation of PDMS/Si substrate during deposition [46], which enables easier atom spreading across its surface and consequently leads to larger particles and a more regular appearance. Consequently, samples on PDMS/Si exhibit lower roughness compared to those composed solely of PDMS (as shown in Table 1). Notably, when the deposition pressure exceeds 1.0 Pa, the PDMS/Si folded wavelength measurement exceeds 50 μm, and the corresponding amplitude is too small to be used for evaluation purposes.

3.2. Crystal structure of the deposited metal films

The crystal structure of metal films can significantly impact their chemical activity, resulting in variations in interfacial interactions and wetting behaviors with LMs. Fig. 3 illustrates the X-ray diffraction (XRD) patterns of the metal films deposited on both PDMS and PDMS/Si substrates. Both Cu films on PDMS and PDMS/Si exhibit a polycrystalline structure characterized by a face-centered cubic lattice (FCC), displaying mixed reflections of (111), (200), and (220) corresponding to the FCC Cu phase [54–56]. No discernible diffraction peak associated with Ti is observed, possibly due to its relatively thin thickness.

The integrated areas of Cu(111) and Cu(200) on PDMS and PDMS/Si substrates, as well as their ratio ($I_{(111)}/I_{(200)}$), are presented in Fig. 4. Here, $I_{(111)}$ is defined as the integral area of the Cu (111) peak and $I_{(200)}$ as the integral area of the Cu (200) peak. $I_{(111)}/I_{(200)}$ indicates the degree of optimization of the Cu film for the orientation of the (111) crystal [57]. On the PDMS substrate, $I_{(111)}$ of Cu films decreases gradually with increasing deposition pressure. While, on the PDMS/Si substrate, $I_{(111)}$ drops sharply at 1.0 Pa and then slowly decreases with increasing deposition pressure. In addition, on both substrates, $I_{(111)}/I_{(200)}$ ratio shows a gradual increase in and then declines with increasing deposition pressure. The $I_{(111)}/I_{(200)}$ ratio on the PDMS substrate decreases significantly at 2.0 Pa, while the ratio remains stable after 2.0 Pa for the PDMS/Si samples. For the PDMS sample (Fig. 4(a)), the peak $I_{(111)}/I_{(200)}$ ratio of the Cu film covered with PDMS at a pressure of 1.0 Pa was found to be 5.46, surpassing the initial value of 4.94 at 0.5 Pa. However, this ratio decreased to a minimum value of 1.88 when the pressure was increased to 2.5 Pa. In contrast, for the PDMS/Si substrate (Fig. 4(b)), as the pressure increased from 0.5 Pa to 1.5 Pa, there was an increase in $I_{(111)}/I_{(200)}$, reaching its maximum value of 4.21 before decreasing to 3.16 at 2.5Pa. It is obvious from Fig. 4 that the $I_{(111)}$ value of PDMS/Si is greater than that of PDMS under each deposition pressure. This indicates that Cu films on PDMS/Si have better crystallinity. In addition, from $I_{(111)}/I_{(200)}$, the Cu film on PDMS/Si shows a more obvious Cu(111) crystal orientation than that of PDMS at high deposition pressure. In addition, theoretical calculations show that the surface energy of Cu(111) is about 1.793 J/m^2 [58], and the surface energy of Cu(200) is about 1.081 J/m^2 [59]. It is obvious that the activity of Cu (111) is higher than that of Cu(200).

3.3. Wetting behavior of LMs

The contact angle of EGaIn liquid on different samples is illustrated in Fig. 5. LMs exhibit superior wetting characteristics on PDMS/Si samples compared to PDMS substrates. On the PDMS substrate, the contact angle of LMs increases from 33.4° to 79.5° with increasing deposition pressure. In contrast, on PDMS/Si test samples, the contact angle initially decreases to 19.0° at 1.5 Pa and then gradually increases as deposition pressure rises.

The morphology and composition of the wetted samples were investigated using scanning electron microscopy (SEM) and energy dispersive spectroscopy (EDS), revealing the interface characteristics

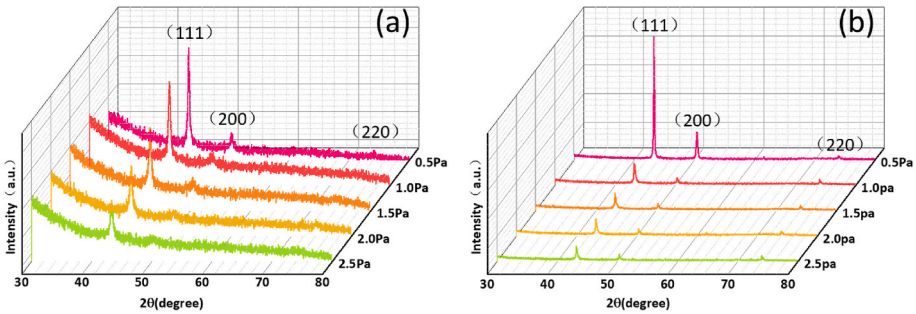

Fig. 3. XRD pattern of Cu films on (a) PDMS and (b) PDMS/Si.

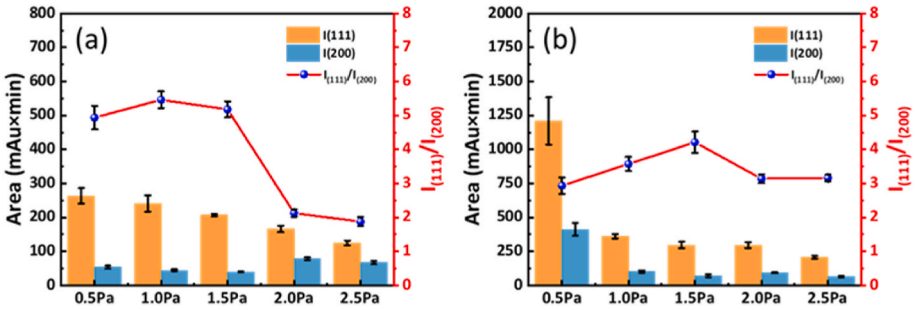

Fig. 4. The $I_{(111)}$, $I_{(200)}$ and $I_{(111)}/I_{(200)}$ on (a) PDMS, (b) PDMS/Si.

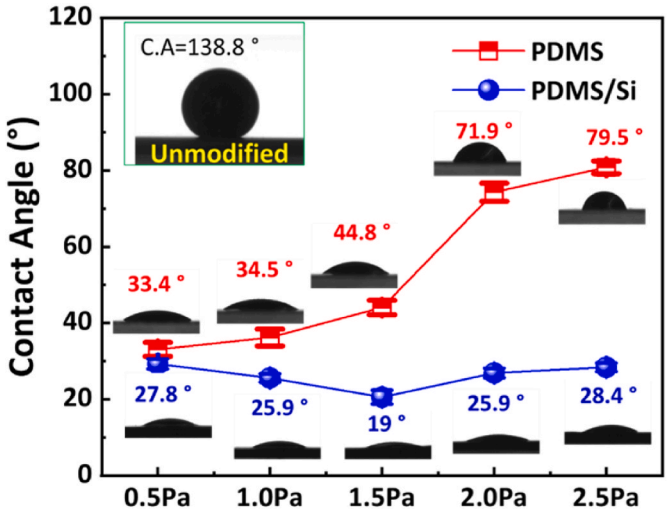

Fig. 5. LMs contact angle for samples on PDMS and PDMS/Si substrates.

and structural evolution. Fig. 6 illustrates three distinct regions on the wet surface of the PDMS/Si sample at 1.5 Pa. Region I corresponds to an excess EGaIn region, where LMs can be detected. The energy spectrum demonstrates an enrichment of Ga and In elements in this region, with a few scattered Cu atoms present. Region II represents the transitional area of the wetting reaction, exhibiting white crystals nearby. The EDS reveals an overlap of Cu and Ga elements in Region II, indicating their wetting reaction. Additionally, some weak In element signals appear in the area adjacent to Region I, suggesting slight infiltration of EGaIn. Notably, the Cu element shows significant enrichment during EDS analysis while Ga and In elements are absent in this region, strongly indicating that LMs did not reach zone III during the wetting test , thus confirming it as an unreacted area.

The high-resolution transmission electron microscopy (HRTEM) images of the metal film before and after the wetting test, as well as the energy dispersive X-ray energy spectrometry (EDS) results of the sample's cross-sectional area, selective area electron diffraction (SAED) image in region II, and X-ray diffraction (XRD) data are presented in Fig. 7. Analysis of Fig. 7(a) and (b) reveals that the grain size of the films is approximately 40 nm before wetting testing, which increases to over 200 nm post-wetting testing. In detail, Figs. 7(b-1) and (b-2) show the electron diffraction patterns from TEM after wetting test. By comparing the calibration of the electron diffraction patterns with the international centre for diffraction data (ICDD) (Fig. 7(d)), the $CuGa_2$ was determined in the wetting area. EDS imaging in Fig. 7(c) confirms only the presence of Cu and Ga elements within the transition region's cross-section, with no evidence of In elements detected. This further supports that the reaction between Cu thin films and LMs exclusively involves Cu and Ga atoms. Additionally, Fig. 7(c)'s nanoscale Ti transition layer affirms excellent stability between PDMS and LMs. Based on X-ray diffraction analysis from region II in Fig. 7(d), it can be concluded that the diffraction intensity of $CuGa_2$ significantly surpasses that of the Cu layer, providing further confirmation that $CuGa_2$ is a product resulting from wetting reactions.

3.4. Discussion on LMs wetting mechanism

It is widely acknowledged that the chemical composition and surface morphology of materials exert a crucial influence on their wetting behavior [60–62]. The wetting behavior of LMs seems to be affected by the chemical reaction between the Cu film and LMs [63], as evidenced by the interfacial characteristics and structural evolution depicted in Figs. 6 and 7. Moreover, following the Cassie model [64], when a droplet adheres to a surface, air occupies the gaps between micro-convex bodies or on the surface. These air-filled gaps diminish the effective contact area, ultimately resulting in a hydrophobic state.

In comparison to PDMS, the wettability of LMs on PDMS/Si samples surpasses it, as evidenced by the surface morphology (Fig. 2), the crystal structure of the Cu layer (Fig. 4), and wetting results (Fig. 5). Both PDMS and PDMS/Si samples exhibit unidirectional wrinkle structures on their surfaces at a pressure of 0.5 Pa, which hinders air bubble capture and promotes the reaction between LMs and Cu resulting in a low contact angle. However, as the deposition pressure increases, the PDMS sample surface exhibits a quadrilateral shape, which may effectively entrap air

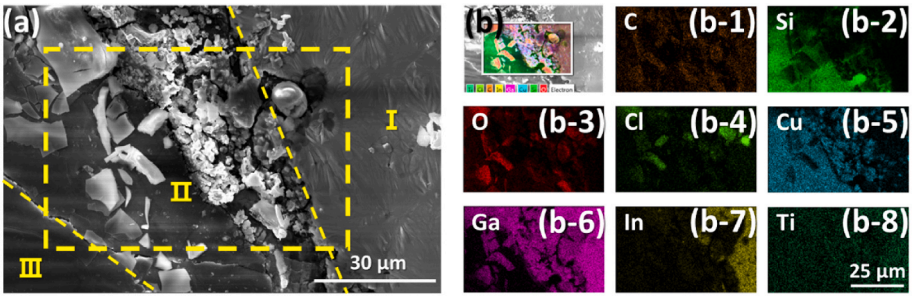

Fig. 6. (a) SEM images of the wet surface of PDMS/Si sample at 1.5 Pa,(b)EDS spectrum in Region II.

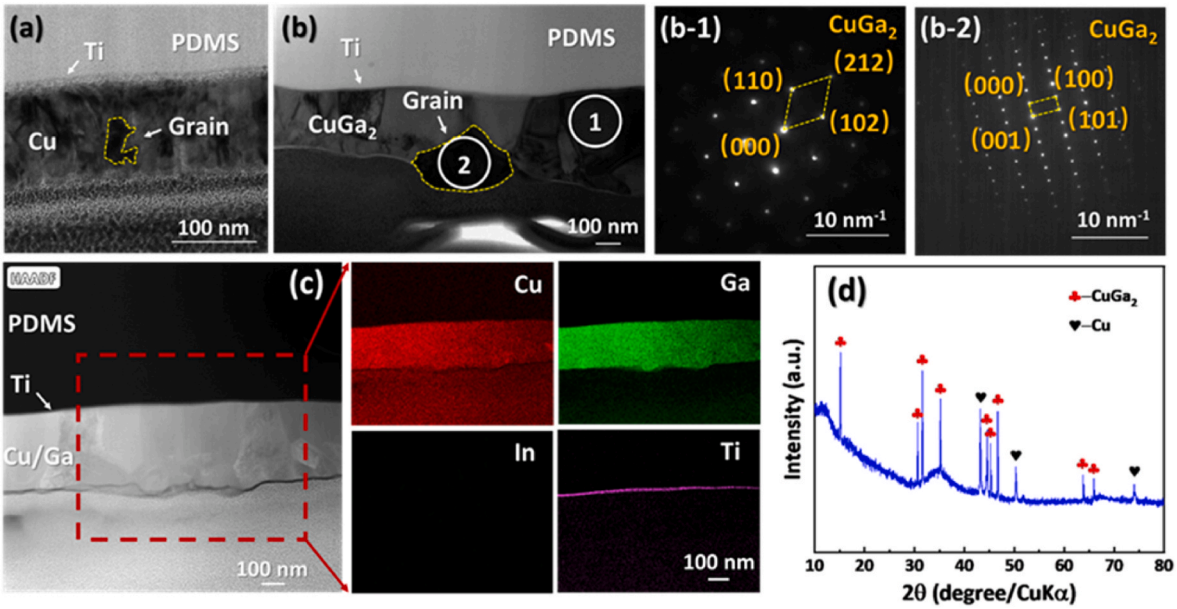

Fig. 7. The cross-sectional images of the Cu layer before (a) and after wetting test (b), (b-1), and (b-2) are the selected area electron diffraction patterns; (c) The cross-sectional HAADF image of the region II and EDS spectrum; (d) XRD pattern from the region II after wetting test.

bubbles. Moreover, elevated deposition pressures lead to the proliferation of more surface cracks. Additionally, owing to the absence of a rigid substrate beneath the PDMS, the metal film exhibits high sensitivity and may form minute cracks under bending, stretching, or contact with the sample [65]. Along these crack sites, the liquid metal can enter into and contact with the exposed PDMS. The contact area between liquid metal and Cu films diminishes, while more liquid metal would contact with PDMS. These combined factors may result in a reduced actual contact area between the liquid metal and Cu films, leading to an increased contact angle. We will call this model I as shown in Fig. 8. The wetting behavior of liquid metal on PDMS/Si samples is influenced by the crystal structure of the Cu layer under deposition pressure ranging from 1.0 to 2.5 Pa. It should be noted that a clear correlation between the contact angle and the $I_{(111)}/I_{(200)}$ ratio emerges when the surface flatness is ensured, possibly due to the enhanced wetting reaction resulting from Ga atom diffusion on Cu(111). We will call this model II as shown in Fig. 8.

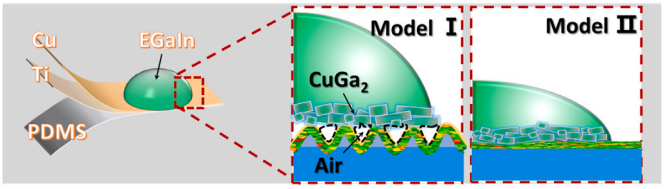

Fig. 8. Schematic diagram of the wetting mechanism of gallium-based liquid metal on Cu films.

4. Conclusion

In this study, we manipulated the surface microstructure and morphology of a Cu film to investigate its influence on the wettability of EGaIn liquid metals. The wettability of EGaIn was observed to range from 19° to 79.5° as a result. This variation in wettability can be attributed to the chemical reaction between the Cu layer and EGaIn, with $CuGa_2$ identified as the primary reaction product. The presence of entrapped air bubbles on surfaces exhibiting wrinkled structures reduces the effective contact area between LMs and Cu, increasing the contact angle. Conversely, smooth surfaces with a higher $I_{(111)}/I_{(200)}$ ratio in the Cu layer facilitate Ga atom diffusion and promote wetting reactions. Our research provides valuable insights into how surface modifications can significantly impact the wettability properties of LM-based systems, thereby holding great potential for various applications.

CRediT authorship contribution statement

Jianxiao Shen: Writing – original draft, Visualization, Investigation, Formal analysis, Data curation, Conceptualization. **Peng Guo:** Writing – review & editing, Visualization, Project administration, Investigation, Funding acquisition, Conceptualization. **Shiying Li:** Software, Investigation. **Wei Yang:** Software, Investigation. **Cheng Zhang:** Writing – review & editing. **Aiying Wang:** Writing – review & editing, Visualization, Resources, Project administration, Funding acquisition.

Declaration of competing interest

The authors declare that they have no known competing financial interests or personal relationships that could have appeared to influence the work reported in this paper.

Data availability

The data that has been used is confidential.

Acknowledgment

This research was supported by the National Natural Science Foundation of China (U20A20296, 52127803) and the Science and Technology Innovation 2025 Major Project of Ningbo (2023Z021). The authors would like to express their gratitude to Dr. Zhou Guangxue and Professor Li Runwei from the Ningbo Institute of Materials Technology and Engineering, Chinese Academy of Sciences, for their valuable discussions and comments.

References

[1] X. Dou, H. Wang, Z. Liu, B. Zheng, Z. Zheng, X. Liu, R. Guo, Epoxy resin-assisted Cu catalytic printing for flexible Cu conductors on smooth and rough substrates, ACS Appl. Mater. Interfaces 15 (44) (2023) 51915–51925.

[2] S. Yan, G. Zhang, H. Jiang, F. Li, L. Zhang, Y. Xia, Z. Wang, Y. Wu, H. Li, Highly stretchable room-temperature self-healing conductors based on wrinkled graphene films for flexible electronics, ACS Appl. Mater. Interfaces 11 (11) (2019) 10736–10744.

[3] M. Nie, B. Li, Y.L. Hsieh, K.K. Fu, J. Zhou, Stretchable one-dimensional conductors for wearable applications, ACS Nano 16 (12) (2022) 19810–19839.

[4] W. Hou, Q.W. Liao, S. Xie, Y.J. Song, L. Qin, Prospects and challenges of flexible stretchable electrodes for electronics, Coatings 12 (5) (2022).

[5] Y.M. Wang, X.S. Li, Y. Hou, C.R. Yin, Z.X. Yin, A review on structures, materials and applications of stretchable electrodes, Front. Mater. Sci. 15 (1) (2021) 54–78.

[6] S. Yao, Y. Zhu, Nanomaterial-enabled stretchable conductors: strategies, materials and devices, Adv Mater 27 (9) (2015) 1480–1511.

[7] S. Choi, S.I. Han, D. Kim, T. Hyeon, D.H. Kim, High-performance stretchable conductive nanocomposites: materials, processes, and device applications, Chem. Soc. Rev. 48 (6) (2019) 1566–1595.

[8] W. Wu, Stretchable electronics: functional materials, fabrication strategies and applications, Sci. Technol. Adv. Mater. 20 (1) (2019) 187–224.

[9] N. Matsuhisa, X. Chen, Z. Bao, T. Someya, Materials and structural designs of stretchable conductors, Chem. Soc. Rev. 48 (11) (2019) 2946–2966.

[10] P. Li, Y. Zhang, Z. Zheng, Polymer-assisted metal deposition (PAMD) for flexible and wearable electronics: principle, materials, printing, and devices, Adv Mater 31 (37) (2019) e1902987.

[11] Y. Ma, Y. Zhang, S. Cai, Z. Han, X. Liu, F. Wang, Y. Cao, Z. Wang, H. Li, Y. Chen, X. Feng, Flexible hybrid electronics for digital healthcare, Adv Mater 32 (15) (2020) e1902062.

[12] J.A. Rogers, T. Someya, Y. Huang, Materials and mechanics for stretchable electronics, Science 327 (5973) (2010) 1603–1607.

[13] S. Chen, R. Zhao, X. Sun, H. Wang, L. Li, J. Liu, Toxicity and biocompatibility of liquid metals, Adv. Healthcare Mater. 12 (3) (2023) e2201924.

[14] T. Daeneke, K. Khoshmanesh, N. Mahmood, I.A. de Castro, D. Esrafilzadeh, S. J. Barrow, M.D. Dickey, K. Kalantar-Zadeh, Liquid metals: fundamentals and applications in chemistry, Chem. Soc. Rev. 47 (11) (2018) 4073–4111.

[15] M.D. Dickey, At room temperature, Phys. Today 74 (4) (2021) 30–36.

[16] Q. Wang, Y. Yu, J. Liu, Preparations, characteristics and applications of the functional liquid metal materials, Adv. Eng. Mater. 20 (5) (2018).

[17] M. Baharfar, K. Kalantar-Zadeh, Emerging role of liquid metals in sensing, ACS Sens. 7 (2) (2022) 386–408.

[18] S.C. Hardy, The surface-tension of liquid gallium, J. Cryst. Growth 71 (3) (1985) 602–606.

[19] T.Y. Liu, P. Sen, C.J.C.J. Kim, Characterization of nontoxic liquid-metal alloy galinstan for applications in microdevices, J. Microelectromech. Syst. 21 (2) (2012) 443–450.

[20] X. Zhao, S. Xu, J. Liu, Surface tension of liquid metal: role, mechanism and application, Front. Energy 11 (4) (2017) 535–567.

[21] C.M. Hansen, New simple method to measure polymer surface tension, Pigment Resin Technol. 27 (6) (1998) 374–378.

[22] G.T. Dee, B.B. Sauer, The surface tension of polymer liquids, Adv. Phys. 47 (2) (1998) 161–205.

[23] K. Szymczyk, A. Zdziennicka, J. Krawczyk, B. Janczuk, Wettability, adhesion, adsorption and interface tension in the polymer/surfactant aqueous solution system. I. Critical surface tension of polymer wetting and its surface tension, Colloid. Surface. 402 (2012) 132–138.

[24] Y. Tian, M. Ina, Z. Cao, S.S. Sheiko, A.V. Dobrynin, How to measure work of adhesion and surface tension of soft polymeric materials, Macromolecules 51 (11) (2018) 4059–4067.

[25] A. Zdziennicka, J. Krawczyk, K. Szymczyk, B. Janczuk, Components and parameters of liquids and some polymers surface tension at different temperature, Colloid. Surface. 529 (2017) 864–875.

[26] T.V. Neumann, M.D. Dickey, Liquid metal direct write and 3D printing: a review, Advanced Materials Technologies 5 (9) (2020).

[27] D.P. Parekh, C.M. Fancher, M.G. Mohammed, T.V. Neumann, D. Saini, J. Guerrier, C. Ladd, E. Hubbard, J.L. Jones, M.D. Dickey, Liquid–solid mixtures of Ga metal infused with Cu microparticles and nanoparticles for microscale and nanoscale patterning of solid metals at room temperature, ACS Appl. Nano Mater. 3 (12) (2020) 12064–12070.

[28] N. Lazarus, S.S. Bedair, I.M. Kierzewski, Ultrafine pitch stencil printing of liquid metal alloys, ACS Appl. Mater. Interfaces 9 (2) (2017) 1178–1182.

[29] W. Lv, Z. Liu, Z. Li, Z. Han, Y. Yang, Q. Li, Y. Qiao, Y. Song, Flexible substrates enabled highly integrated patterns with submicron precision toward intrinsically stretchable circuits, SmartMat 3 (3) (2022) 503–512.

[30] T.H. Park, J.H. Kim, S. Seo, Facile and rapid method for fabricating liquid metal electrodes with highly precise patterns via one-step coating, Adv. Funct. Mater. 30 (35) (2020).

[31] M.D. Dickey, R.C. Chiechi, R.J. Larsen, E.A. Weiss, D.A. Weitz, G.M. Whitesides, Eutectic gallium-indium (EGaIn): a liquid metal alloy for the formation of stable structures in microchannels at room temperature, Adv. Funct. Mater. 18 (7) (2008) 1097–1104.

[32] K. Khoshmanesh, S.Y. Tang, J.Y. Zhu, S. Schaefer, A. Mitchell, K. Kalantar-Zadeh, M.D. Dickey, Liquid metal enabled microfluidics, Lab Chip 17 (6) (2017) 974–993.

[33] Y. Lin, O. Gordon, M.R. Khan, N. Vasquez, J. Genzer, M.D. Dickey, Vacuum filling of complex microchannels with liquid metal, Lab Chip 17 (18) (2017) 3043–3050.

[34] A. Hirsch, L. Dejace, H.O. Michaud, S.P. Lacour, Harnessing the rheological properties of liquid metals to shape soft electronic conductors for wearable applications, Acc. Chem. Res. 52 (3) (2019) 534–544.

[35] A. Hirsch, S.P. Lacour, A method to form smooth films of liquid metal supported by elastomeric substrate, Adv. Sci. 5 (10) (2018) 1800256.

[36] A. Hirsch, H.O. Michaud, A.P. Gerratt, S. de Mulatier, S.P. Lacour, Intrinsically stretchable biphasic (Solid-Liquid) thin metal films, Adv Mater 28 (22) (2016) 4507–4512.

[37] Y.R. Jeong, J. Kim, Z.Q. Xie, Y.G. Xue, S.M. Won, G. Lee, S.W. Jin, S.Y. Hong, X. Feng, Y.G. Huang, J.A. Rogers, J.S. Ha, A skin-attachable, stretchable integrated system based on liquid GaInSn for wireless human motion monitoring with multi-site sensing capabilities, NPG Asia Mater. 9 (10) (2017) e443.

[38] Y.B. Jiang, S.K. Su, H.R. Peng, H.S. Kwok, X. Zhou, S.M. Chen, Selective wetting/dewetting for controllable patterning of liquid metal electrodes for all-printed device application, J. Mater. Chem. C 5 (47) (2017) 12378–12383.

[39] M.G. Kim, C. Kim, H. Alrowais, O. Brand, Multiscale and uniform liquid metal thin-film patterning based on soft lithography for 3D heterogeneous integrated soft microsystems: additive stamping and subtractive reverse stamping, Advanced Materials Technologies 3 (7) (2018).

[40] G. Li, D.W. Lee, An advanced selective liquid-metal plating technique for stretchable biosensor applications, Lab Chip 17 (20) (2017) 3415–3421.

[41] J.H. Kim, S. Kim, H. Kim, S. Wooh, J. Cho, M.D. Dickey, J.H. So, H.J. Koo, Imbibition-induced selective wetting of liquid metal, Nat. Commun. 13 (1) (2022) 4763.

[42] N. Abid, A.M. Khan, S. Shujait, K. Chaudhary, M. Ikram, M. Imran, J. Haider, M. Khan, Q. Khan, M. Maqbool, Synthesis of nanomaterials using various top-down and bottom-up approaches, influencing factors, advantages, and disadvantages: a review, Adv. Colloid Interface Sci. 300 (2022) 102597.

[43] P.J. Kelly, R.D. Arnell, Magnetron sputtering: a review of recent developments and applications, Vacuum 56 (3) (2000) 159–172.

[44] B. Hu, X.-L. Shi, T. Cao, M. Li, W. Chen, W.-D. Liu, W. Lyu, T. Tesfamichael, Z.-G. Chen, Advances in flexible thermoelectric materials and devices fabricated by magnetron sputtering, Small Science (2023).

[45] Q. Jin, W. Shi, Y. Zhao, J. Qiao, J. Qiu, C. Sun, H. Lei, K. Tai, X. Jiang, Cellulose fiber-based hierarchical porous bismuth telluride for high-performance flexible and tailorable thermoelectrics, ACS Appl. Mater. Interfaces 10 (2) (2018) 1743–1751.

[46] S.J. Li, K. Wu, H.Z. Yuan, J.Y. Zhang, G. Liu, J. Sun, Formation of wrinkled patterns in metal films deposited on elastic substrates: tunability and wettability, Surf. Coating. Technol. 362 (2019) 35–43.

[47] N. Bowden, S. Brittain, A.G. Evans, J.W. Hutchinson, G.M. Whitesides, Spontaneous formation of ordered structures in thin films of metals supported on an elastomeric polymer, Nature 393 (6681) (1998) 146–149.

[48] X.M. Li, D. Reinhoudt, M. Crego-Calama, What do we need for a superhydrophobic surface? A review on the recent progress in the preparation of superhydrophobic surfaces, Chem. Soc. Rev. 36 (8) (2007) 1350–1368.

[49] S. Wang, K. Liu, X. Yao, L. Jiang, Bioinspired surfaces with superwettability: New insight on theory, design, and applications, Chem Rev 115 (16) (2015) 8230–8293.

[50] K. Efimenko, M. Rackaitis, E. Manias, A. Vaziri, L. Mahadevan, J. Genzer, Nested self-similar wrinkling patterns in skins, Nat. Mater. 4 (4) (2005) 293–297.

[51] S. Yu, Y. Sun, Y. Ni, X. Zhang, H. Zhou, Controlled Formation of surface patterns in metal films deposited on elasticity-gradient PDMS substrates, ACS Appl. Mater. Interfaces 8 (8) (2016) 5706–5714.

[52] K.Y. Chan, B.S. Teo, Effect of Ar pressure on grain size of magnetron sputter-deposited Cu thin films, IET Sci. Meas. Technol. 1 (2) (2007) 87–90.

[53] K.Y. Chan, B.S. Teo, Sputtering power and deposition pressure effects on the electrical and structural properties of copper thin films, J. Mater. Sci. 40 (22) (2005) 5971–5981.

[54] C.L. Lin, P.S. Chen, C.L. Chang, M.C. Chen, Characteristics of copper films deposited on H -plasma-treated TaN substrate by chemical vapor deposition, J Vac Sci Technol B 20 (5) (2002) 1947–1953.

[55] K. Kamoshida, Y. Ito, Highly preferred (111) texture aluminum-copper films formed with argon plasma treatment of the titanium underlayer and their electromigration endurance as interconnects, J Vac Sci Technol B 15 (4) (1997) 961–966.

[56] N. Joshi, A.K. Debnath, D.K. Aswal, K.P. Muthe, M.S. Kumar, S.K. Gupta, J. V. Yakhmi, Morphology and resistivity of Al thin films grown on Si(111) by molecular beam epitaxy, Vacuum 79 (3–4) (2005) 178–185.

[57] S.K. Mukherjee, L. Joshi, P.K. Barhai, A comparative study of nanocrystalline Cu film deposited using anodic vacuum arc and dc magnetron sputtering, Surf. Coating. Technol. 205 (19) (2011) 4582–4595.

[58] Y. Liu, Y. Huang, Z. Xiao, X. Reng, Study of adsorption of hydrogen on Al, Cu, Mg, Ti surfaces in Al alloy melt via first principles calculation, Metals 7 (1) (2017).

[59] Z. Li, J. Feng, Z. Wu, M. Pang, D. Liu, W. Yang, Y. Zhan, The stability and electronic structure of Cu(200)/AuCu(200) interface: an insight from first-principle calculation, Materials 15 (4) (2022).

[60] X.Y. Hu, Z. Tian, C.H. Chen, G.C. Jiang, L.Z. Wang, R. Peng, D.Z. Li, H.J. Zhang, P. X. Fan, M.L. Zhong, Minimizing interface thermal resistance via laser surface micropatterning for enhancing wetting of gallium-based liquid metal with copper, Int. J. Heat Mass Tran. 214 (2023).

[61] W.G. Lin, W.K. Qiu, Y. Tuersun, X. Huang, S. Chu, Ultrastrong spontaneous surface wetting of room temperature liquid metal on treated metal surface, Adv. Mater. Interfac. 8 (18) (2021).

[62] X.Y. Hu, Z. Tian, X. Luo, C.H. Chen, G.C. Jiang, L.Z. Wang, R. Peng, H.J. Zhang, M. L. Zhong, Wetting behavior of gallium-based room temperature liquid metal (LM) on nanosecond-laser-structured metal surfaces, Surface. Interfac. 32 (2022).

[63] Y. Cui, F. Liang, Z. Yang, S. Xu, X. Zhao, Y. Ding, Z. Lin, J. Liu, Metallic bond-enabled wetting behavior at the liquid Ga/CuGa(2) interfaces, ACS Appl. Mater. Interfaces 10 (11) (2018) 9203–9210.
[64] A.B.D. Cassie, S. Baxter, Wettability of porous surfaces, T Faraday Soc 40 (1944) 546–550.
[65] D. Kang, P.V. Pikhitsa, Y.W. Choi, C. Lee, S.S. Shin, L. Piao, B. Park, K.Y. Suh, T. I. Kim, M. Choi, Ultrasensitive mechanical crack-based sensor inspired by the spider sensory system, Nature 516 (7530) (2014) 222–226.